shot noise is lower with a low transmitted intensity. For input power higher than 13 dBm, significant EVM degradation occurs as the peak voltage amplitude of the input 802.11a signal reaches V_π of the EOM and therefore explores another nonlinear part of the EOM static characteristic. As expected by theoretical considerations about mixing with EOM [7], mixing power is higher when working at an LO power of 11 dBm instead of 7 dBm. Optimal LO power of 18.4 dBm would theoretically give even better EVM measurements, which shows a very efficient process for WLAN 802.11a frequency conversion. Figure 7 shows the lowest EVM measurements around 1.4% rms over all the 52 subcarriers of the up-converted 802.11a signal around 5.8 GHz for P_{IF} = 5 dBm and P_{LO} = 11 dBm.

5. CONCLUSION

In this paper, the performance of optical frequency conversion of a WLAN 802.11a signal centered at f_{IF} is studied. Two optical frequency converters are compared: direct modulation of a LD and the use of a standard EOM. Both devices are biased in nonlinear regimes. Spectrum analysis has been investigated. It has been shown that a twice wider available conversion bandwidth of $2f_{IF}$ can be obtained with EOM compared to LD mixing technique as LO is rejected in the RF photodetected output spectrum.

Constellation diagrams for both mixing techniques have reported symmetrical constellation without any distortion caused by frequency up-conversion. EVM measurements of the up-converted 802.11a signal have shown low degradation caused by both optical mixing techniques compared to direct detection in the RoF link. The LD mixing technique offers cost effective 802.11a frequency conversion solution with high mixing power but with limited available bandwidth and small input power range from −5 dBm to 0 dBm, considering that bias current of the LD has to be set to a constant value.

Lowest values of EVM are obtained with EOM mixing technique at minimum of transmission as the shot noise is minimum with low transmitted intensity. For EOM, the range of optimal 802.11a input power is large, from −7 dBm up to 13 dBm. In this range, EVM measurements are lower than 3% rms, optimal input powers of P_{IF} = 5 dBm and P_{LO} = 11 dBm lead to a very low EVM value of 1.4% rms, which shows a degradation of only 0.1% compared to direct optical transmission without frequency conversion.

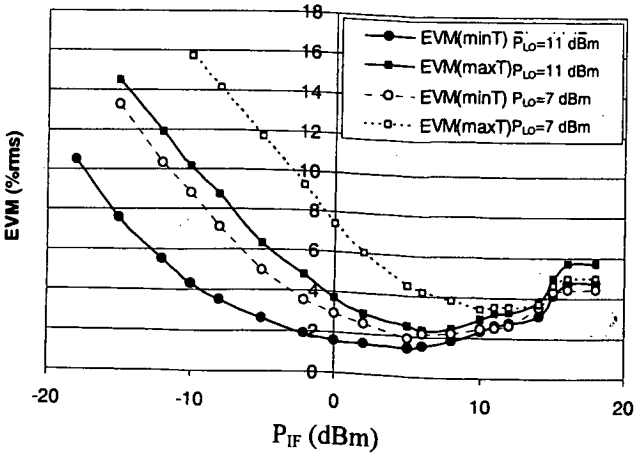

Figure 6 EVM measurement of the up-converted 802.11a signal with tl

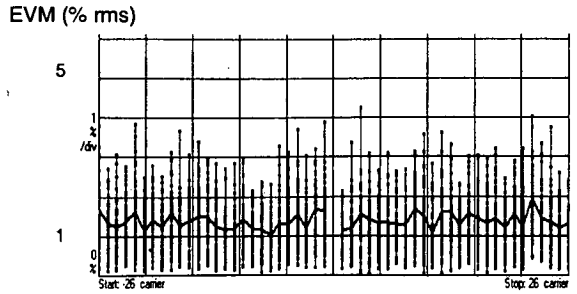

Figure 7 Constellation of the up-converted 802.11a signal at 5.8 GHz with EOM at MinT with P_{IF} = 5 dBm and P_{LO} = 11 dBm

REFERENCES

1. F. Gruson, G. Gaborit, P. Abele, and H. Schumacher, A broadband SiGe mixer for 5-GHz WLAN applications with X-band quadrature generation and high image-rejection, IEEE Radio Freq Integrated Circ Symp, Fort Worth, TX, 2004, pp. 523–526.
2. H.-J. Song, J.S. Lee, and J.-I. Song, All-optical harmonic frequency up-conversion for a WDM radio over fiber system, IEEE MTT-S Int Microwave Symp Dig 1 (2004), 405–407.
3. T. Ismail and A.J. Seeds, Feed-forward linearization of directly modulated laser for radio over fibre wireless LAN, 2nd Euro Nefertiti Winter School Microwave Photon, York, England, 2004.
4. G.K. Gopalakrishnan, W.K. Burns, and C.H. Bulmer, Microwave-optical mixing in $LiNbO_3$ modulators, IEEE Trans Microwave Theory Tech 43 (1995), 2357–2360.
5. P.K. Tang, L.C. Ong and al. PER and EVM measurements of a radio-over-fiber network for cellular and WLAN system applications, IEEE J Lightwave Technol 22 (2004), 2370–2376.
6. H. Ogawa and Y. Kamiya, Fiber-optic microwave transmission using harmonic laser mixing, optoelectronic mixing, and optically pumped mixing, IEEE Trans Microwave Theory Tech 39 (1991), 2045–2051.
7. Y. Le Guennec, G. Maury, and B. Cabon, BER performance comparison between active Mach–Zehnder modulator and passive Mach–Zehnder interferometer for conversion of microwave subcarriers of BPSK signals, Microwave Opt Technol Lett (2003), 496–498.

CALCULATION OF ANTENNA ARRAY FAR FIELD IMPULSE RESPONSE USING THE FINITE-DIFFERENCE TIME-DOMAIN METHOD

Chen Wu and Jim Lee
Defense Research and Development Canada–Ottawa
3701 Carling Ave.
Ottawa, Canada, K1A 0Z4

Received 30 August 2005

ABSTRACT: *The waveform in the radiation field of a radar antenna can be obtained by using the convolution of the transmitted signal and the antenna far-field impulse response (AFFIR). In this paper, the finite-difference time-domain (FDTD) method is applied to calculate the AFFIR of an X-band 54-element waveguide slot array at different radiation angles using the excitation of a wideband Gaussian pulse. To demonstrate the usage of the far-field impulse response, the waveforms in the radiation field of a narrowband Gaussian pulse are calculated at three different radiation angles by the convolution of the pulse and the waveguide slot-array AFFIR.* © 2006 Wiley Periodicals, Inc. Microwave Opt Technol Lett 48: 424–430, 2006; Published online in Wiley InterScience (www.interscience.wiley.com). DOI 10.1002/mop.21370

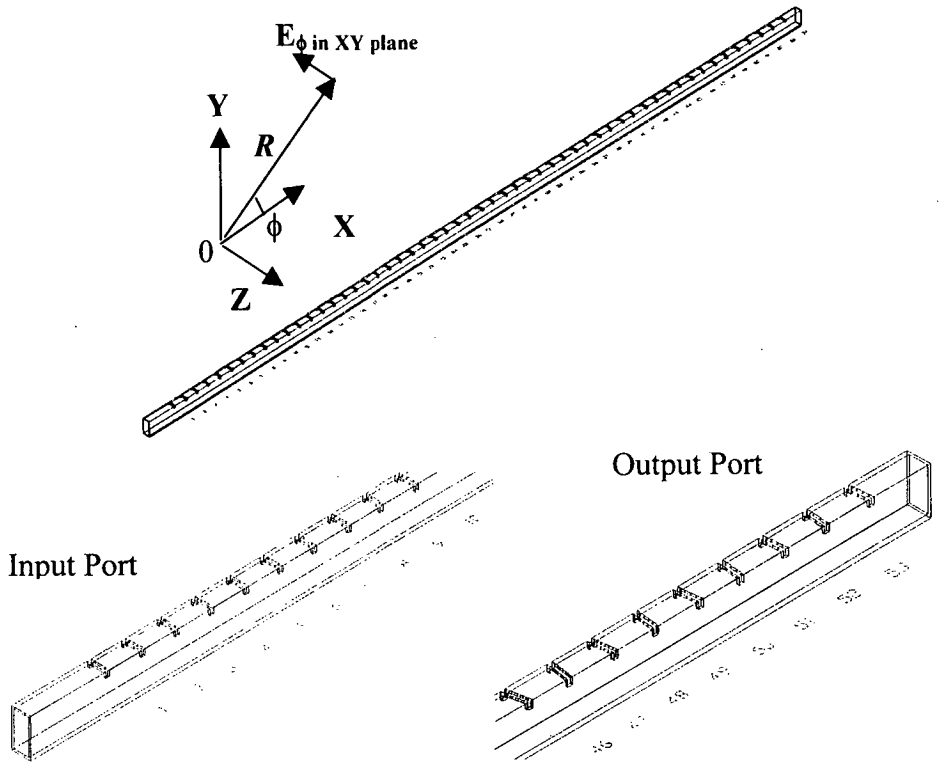

Figure 1 Isometric views of the 54-element waveguide slot array

Key words: *finite-difference time-domain; slot waveguide array; impulse response; antenna far field*

1. INTRODUCTION

In order to obtain a better understanding how a radar-antenna structure affects the characteristics of a radiated signal, the transient effects of the electromagnetic field [1, 2] associated with the pulsed signals need to be investigated. An array far-field impulse response (AFFIR) [3] can be used as a function of radiation angle to model these effects because it represents the array spatial and temporal radiation characteristics. Since the FDTD method [4–6] models the electromagnetic problems in both the spatial and temporal domains, it can straightforwardly model radar pulses propagating in an antenna, which may have a very complex structure. However, to investigate the characteristics of different radar pulses radiated by an antenna array, its AFFIR has to be obtained. Since it is very difficult to measure an AFFIR at any radiation angle, in this paper, we demonstrate how to compute the AFFIR using the FDTD method and time-domain near-to-far-field transformation. An X-band 54-element waveguide slot array, which is a part of shipborne navigation radar, is modeled by the FDTD method. Using the model, the wideband Gaussian pulse is excited at the input port of the array, and its time-domain far fields (after time-domain near-to-far-field transformation) are calculated at different radiation angles. Then a Matlab® program utilizes the time-domain far-field results and the wideband Gaussian pulse to determine the AFFIR. To demonstrate the accuracy of the Matlab® program and usage of AFFIR, the far-field waveforms of a narrowband Gaussian pulse is calculated in three directions by taking the following approaches:

1. using the convolution of the narrowband Gaussian pulse and calculated AFFIR of the waveguide slot array;
2. the narrowband Gaussian pulse is launched at the input port of the waveguide slot array, and its far-field waveforms are calculated directly using the FDTD model and the time-domain near-to-far-field transformation [6].

The far-field waveforms that are obtained by these two approaches agree very well. The method developed in this paper can be applied to obtain the AFFIR of other antenna arrays.

2. WAVEGUIDE SLOT ARRAY AND ITS FDTD MODEL

An X-band 54-element waveguide slot array [7–10] is modeled using the FDTD method. The slots in the array are cut into a narrow wall of a WR-90 waveguide at about 145 mil and wrapped around the adjacent broad walls, so they can be resonant in the X-band. In our FDTD model, the thickness of waveguide wall is 51 mil and the width of the slots is 100 mil. The isometric views of the array are illustrated in Figure 1. One can see that each element is engraved in a different angle. The slot position and angle obliquity determines the amount of power coupled from waveguide. Figure 1 also indicates the following:

1. the signal can be launched from input port, propagates along the waveguide in the X direction, and is radiated by the slots;
2. $\boldsymbol{R}$ (in the X–Y plane) is the distance between the origin and observation point in the far field;
3. ϕ is the angle between the X direction and $\boldsymbol{R}$ in the X–Y plane;
4. the far-field impulse response of E_ϕ in the X–Y plane is calculated as an example in this paper.

The other field components in any radiation angle can be calculated as well.

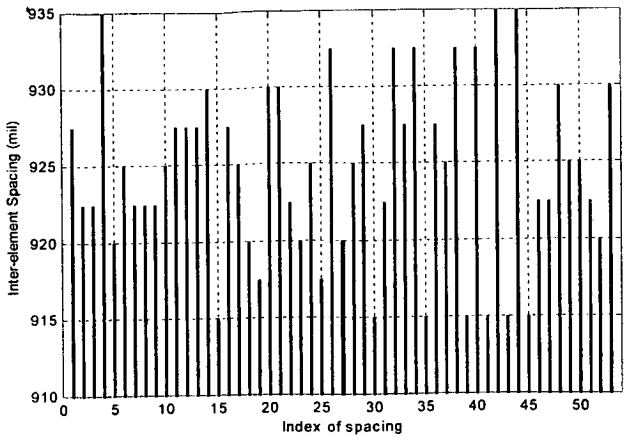

Figure 2 Distances between the centers of adjacent elements in the array

The 53 measured interelement spacings between the centers of the adjacent elements are given in Figure 2. It can be observed that the spacings are slightly different. The average interelement spacing is 924.4 mil. Since the finite-difference scheme is used in the FDTD method, the antenna has to be discretized in the model. The edges of tilted slots are approximated by the staircasings. The detail staircasings of two center elements are shown in Figure 3. In Figure 4 illustrates the mesh setting in the Y–Z plane. An eight-layer perfectly matched layer (PML) [11, 12] absorbing boundary condition is used on the boundaries of the FDTD computational domain to simulate the array in the free space. At both ends of the array, a segment of a uniform WR-90 waveguide is used and terminated by the PML layers. There are 100 grids in the uniform waveguide. The return loss of the eight-layer PML needed to terminate the uniform waveguide is given in Figure 5. The absorbing boundary condition provides excellent termination to simulate a matched generator and load at the input and output ports, respectively. Since the array has a matched load, it is a traveling-wave array [13]. The total grid numbers in the simulation are 5123 × 88 × 57, and mesh sizes are 10 × 17 × 17 mil in the X, Y, and Z directions, respectively. The time step dt is about 0.418 ps.

From Figures 1 and 3, one can observe that the inclination angles (θ) are alternated with respect to the Z-axis of successive elements. For example, θ is less than 90° in the 27th slot, and must be greater than 90° for the 28th slot. The reason for this is to allow fields to be radiated by slots having same phase, since the interelement spacing is around one half-waveguide.

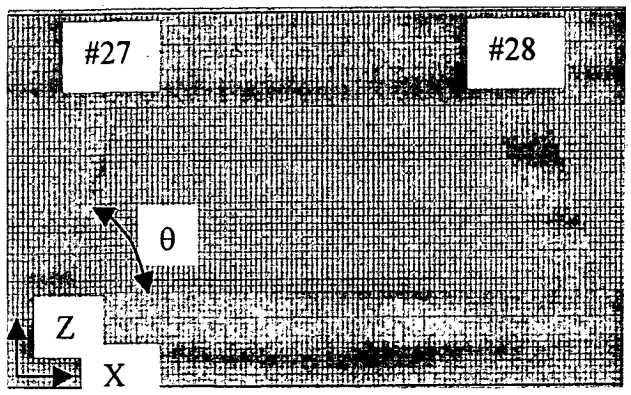

Figure 3 Detailed staircasings of two center elements of the slot array in the FDTD model

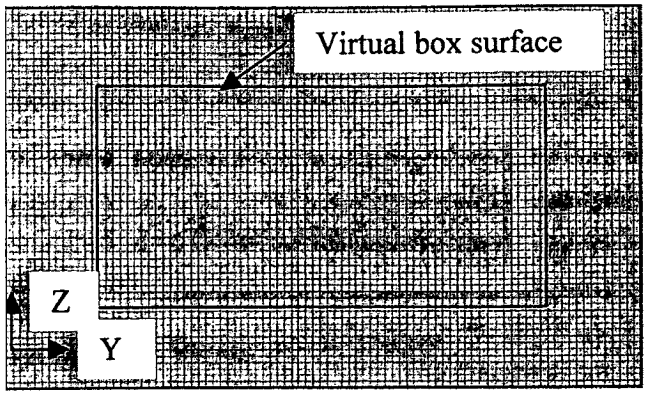

Figure 4 Mesh in the Y–Z plane and the virtual box surfaces parallel to the X-axis

3. WIDEBAND GAUSSIAN PULSE AND FDTD SIMULATION

To obtain the waveguide slot array far field-impulse response, a wideband Gaussian pulse is fed into the array and simulated by the slot-array FDTD model. The spectrum of the pulse is designed in the frequency band, in which WR-90 waveguide fundamental mode is the dominant mode. The pulse and its spectrum are shown in Figure 6. The carrier frequency is 9.41 GHz, which is the navigation-radar center frequency. The excitation plane at the input port is eight grids ahead of the eight-layer PML, and the field distribution in the plane follows the E_z field of waveguide fundamental mode. During the simulation, some data are collected for the post processing. These data are described as follows.

1. The voltages are sampled at the middle of the uniform waveguide, 34 grids before the first slot in the input port, $V_{in}(n\ dt)$, and 50 grids after last slot in the output port $V_{out}(n\ dt)$. Here, n is the time-domain n^{th} iteration in the FDTD simulation.
2. The tangential E-field and H-field on the surfaces of a virtual box, which encloses the slot array, are calculated at 9.41 GHz using discrete Fourier transform (DFT). The surfaces, which are parallel to the X-axis, are located two grids away from the outside walls of the waveguide (Fig. 4). The two end-walls of the virtual box are 80 grids away from the first and last elements at the input and output ports, respectively.
3. In the time domain, the far field, $E_\phi(\phi, t)$, is collected using

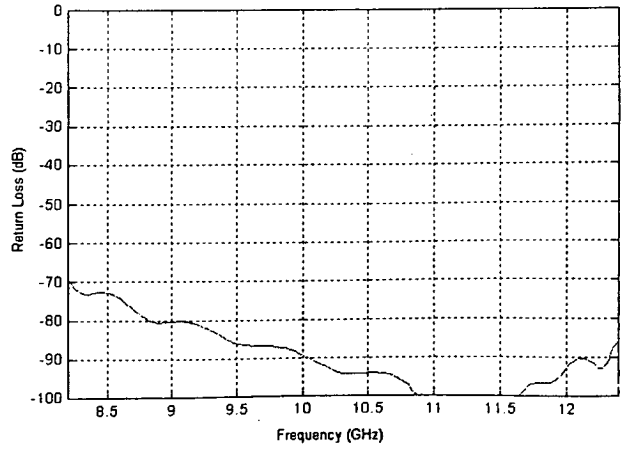

Figure 5 Return loss of an eight-layer PML used to terminate a WR-90 waveguide

 DOI 10.1002/mop

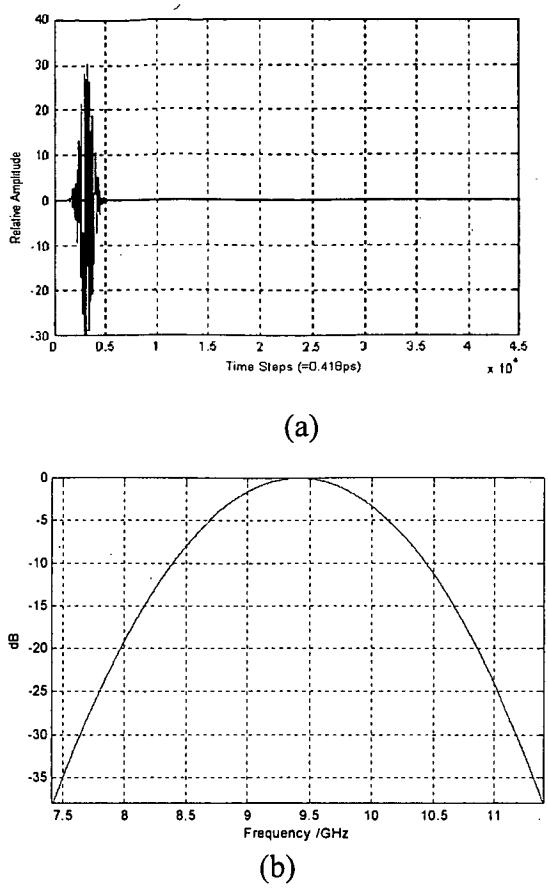

Figure 6 (a) A wideband Gaussian pulse launched into the slot array and (b) its spectrum

the time-domain near-to-far-field transformation. Here, the near fields are the time-domain tangential E-field and H-field on the virtual box surfaces, which are parallel to the X-axis. The tangential fields inside waveguide on the end surfaces of the virtual box are not used in the far-field calculation, since waves inside a waveguide cannot radiate. To save memory, the far fields are collected at every four time steps. The radiation angle ϕ is from 80° to 100° and $\Delta\phi$ equals 0.1°. The time-domain far fields are illustrated in Figure 7. Since the observation points are 10 km away from the center of the array, there is about a 3.33×10^{-5} s time delay when the wave reaches the observation points from the array.

4. S-PARAMETERS OF WAVEGUIDE SLOT ARRAY AND RADIATION PATTERN AT 9.41 GHz

Since the sampling point at the input port is only 34 grids away from the first slot, both the incident and reflected waves are mixed in $V_{in}(n\ dt)$. To separate these signals, the short segment of the uniform waveguide used at the input port of the array is modeled using the FDTD method separately, and the PML is placed on both ends of the short waveguide. The mesh setup and dt are kept the same, as those are used in the slot-array FDTD model. Using the short-waveguide model, the voltage of the incident wave $V_{inc}(n\ dt)$ can be obtained. Thus, S_{11} and S_{21} can be calculated using following equations, as shown in Figure 8:

$$S_{11}(f) = \frac{V_{ref}(f)}{V_{inc}(f)}, \tag{1}$$

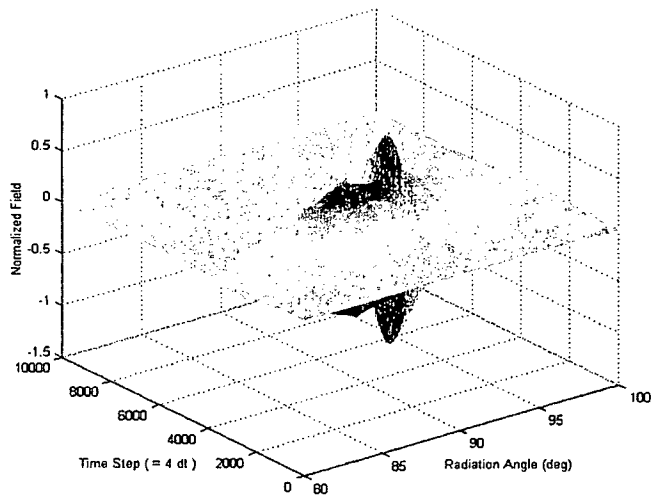

Figure 7 Far-field waveform of $E_\phi(\phi, t)$

$$S_{21}(f) = \frac{V_{tra}(f)}{V_{inc}(f)}, \tag{2}$$

$$V_{ref}(f) = \sum_{n=0}^{N} \{[V_{in}(n\ dt) - V_{inc}(n\ dt)] \cdot \exp(-j2\pi fn\ dt) \cdot dt\}, \tag{3}$$

$$V_{in}(f) = \sum_{n=0}^{N} \{V_{in}(n\ dt) \cdot \exp(-j2\pi fn\ dt) \cdot dt\}, \tag{4}$$

$$V_{tra}(f) = \sum_{n=0}^{N} \{V_{out}(n\ dt) \cdot \exp(-j2\pi fn\ dt) \cdot dt\}, \tag{5}$$

where N equals 70,000. From Figure 8, one can observe the following:

1. return loss is worse than -10 dB at the frequency around 9.147 GHz; this is due to small reflections created by slots, which have approximately the same phase when they reach

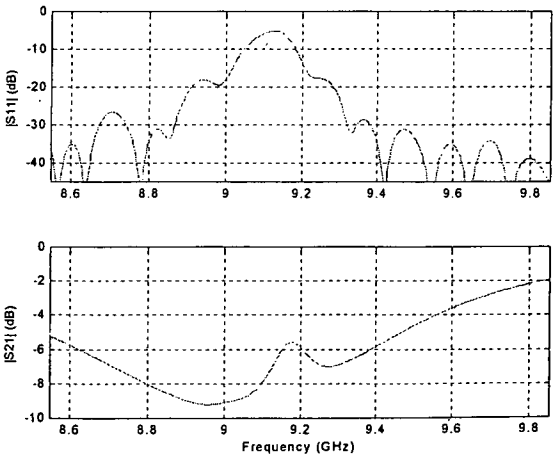

Figure 8 The amplitude of S_{11} and S_{21} of the waveguide slot array

the input port, since the average interelement spacing is equal to the half of waveguide wavelength at 9.147 GHz;
2. $|S_{21}|$ reaches a minimum at 9.014 GHz;
3. $|S_{21}|$ is about -6 dB at 9.41 GHz; this means that about a quarter of the incident power lost at the matched load in the slot-array FDTD model.

Figure 9 shows the far field co- and cross-polarization radiation patterns from 80° to 100°. These patterns are calculated via following approaches:

1. using the 9.41-GHz tangential E-field and H-field on virtual box surfaces parallel to the X-axis, and the frequency-domain near-to-far-field transformation (red line);
2. using the Fourier transform of the far fields in the time domain, $E_\phi(\phi, t)$, as shown in Figure 7 (******).

From the 9.41-GHz far-field radiation patterns, it can be concluded that:

1. the co- and cross-polarizations obtained from above two approaches agree very well;
2. at 9.41 GHz, the array beam points at 87.7° (in the $z = 0$ plane), since the half-waveguide wavelength at this frequency is less than the interelement spacing;
3. the main beamwidth is about 1.7°;
4. the first side-lobe is about 20-dB lower than the main lobe, and the sidelobes are not symmetrical with respect to the main lob;
5. the cross-polarization level is less than -38 dB at the antenna main-beam.

5. ARRAY FAR-FIELD IMPULSE RESPONSE

Using the results given in Figure 7, the far-field impulse response as a function of radiation angle and frequency, $B_\varphi(\phi, f)$, can be calculated as follows:

$$B_\varphi(\phi, f) = \frac{E_\phi(\phi, f)}{G(f)}, \tag{6}$$

$$E_\phi(\phi, f) = \sum_{n=0}^{N} E_\phi(\phi, t) \cdot \exp(-j2\pi f n \Delta t) \cdot \Delta t, \tag{7}$$

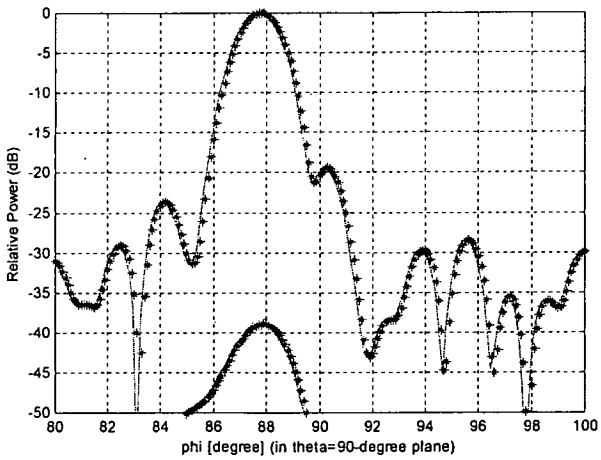

Figure 9 The 9.41-GHz co- and cross-polarization patterns in the $z = 0$ plane

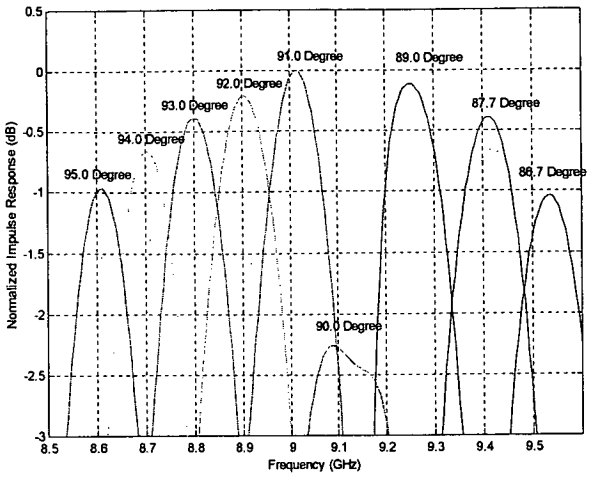

Figure 10 Impulse response of the E_ϕ far field

where $\Delta t = 4dt$, $N = 17500$, and $G(f)$ is the spectrum of the wideband Gaussian pulse shown in Figure 6. Using inverse Fourier transform, the time-domain impulse response, $\mathcal{B}_\varphi(\phi, t)$, can be obtained. To calculate $B_\varphi(\phi, f)$, the spectrum of the wideband Gaussian pulse $G(f)$ is truncated at 7.41 and 11.41 GHz, since the power can be neglected outside the band. From the far-field impulse response $|B_\varphi(\phi, f)|$, as shown in Figure 10, one can find that:

1. at different frequencies, the array beam points at different angles; as the frequency increases, the beam points toward the load end;
2. the efficiency of the array changes at different frequency; the array maximum gain occurs at 9.014 GHz and the beam points at 91°, since it has the lowest power loss at matched load and at the same time a good return loss (~ -20 dB) is achieved (Fig. 8);
3. although the array has a very good return loss (-35 dB) at 9.41 GHz, the gain is still lower than 9.014 GHz because more power is lost at the matched load;
4. at 9.147 GHz, the main-beam points at 90° and the gain is about 2.49-dB lower than 9.014 GHz; the main reason for this is that the return loss is only about -5 dB and $|S_{21}|$ is greater than -6 dB (Fig. 8), so a great amount of the incident wave is reflected and the matched load dissipates more than a quarter of the power carried by the incident wave.

For a uniformly spaced traveling-wave array, the beam-pointing direction ϕ can be calculated by the following equation [13, 14]:

$$\phi = 90 - \arcsin\left(\frac{\lambda}{\lambda_g} - \frac{\lambda}{2S}\right), \tag{8}$$

where λ and λ_g are the free-space and waveguide wavelengths, respectively, and S is the interelement spacing. If an average spacing of 924.43 mil is used, the beam-pointing angles can be calculated versus frequency. Table 1 gives the beam-pointing angles obtained from the AFFIR (Fig. 10) and Eq. (8). One can see that the results given by these two methods are very close to each other. The maximum discrepancy is 0.36°. The nonuniform in-

TABLE 1 Beam-Pointing Angles and Relative Gain at the Beam-Pointing Angles

F [GHz]	Free-Space Wavelength [mil]	TE_{10} Guide Wavelength [mil]	Beam-Pointing Angle [deg]	Beam-Pointing Angle [deg] Eq. (8)	Relative Gain at Beam-Pointing Angle [dB]
8.6095	1370.9	2115.5	95.0	95.36	−0.97
8.7028	1356.2	2062.7	94.0	94.36	−0.65
8.8007	1341.1	2010.7	93.0	93.35	−0.39
8.9037	1325.6	1959.5	92.0	92.32	−0.21
9.0140	1309.4	1908.3	91.0	91.26	0.00
9.1470	1290.4	1850.7	90.0	90.04	−2.49
9.2502	1275.9	1808.9	89.0	89.13	−0.11
9.4100	1254.3	1748.8	87.7	87.77	−0.39
9.5344	1237.9	1705.2	86.7	86.77	−1.04

terelement spacing and the coupling between elements are mainly responsible for the difference.

6. FAR-FIELD WAVEFORMS OF A NARROWBAND GAUSSIAN PULSE

To demonstrate the usage of the AFFIR, a narrowband Gaussian pulse excites the waveguide slot array. The signal and its spectrum are shown in Figures 11(a) and 11(b). During the FDTD simulation, the far-field waveforms are collected in three different angles every four time steps. One of every five sampled data is plotted in the left column of Figure 12. The waveforms on the right column of Figure 12 are calculated using the convolution of the narrowband Gaussian pulse, given in Figure 11, and the AFFIR of waveguide slot array. One can observe that these waveforms (obtained using different approaches) are in very good agreement.

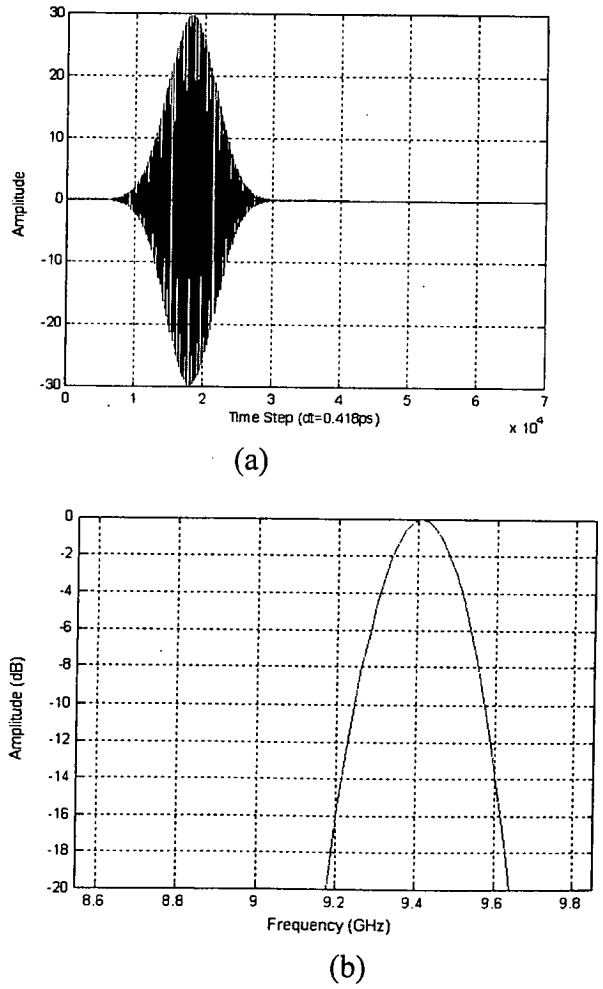

Figure 11 (a) A narrowband Gaussian pulse and (b) its spectrum

7. CONCLUSIONS

This paper has described the calculation of AFFIR as a function of angles using the pulse signal and the corresponding time-domain radiation far fields obtained by the antenna array FDTD model. An X-band 54-element waveguide slot array was used as an example and modeled using the FDTD method. The far-field waveforms at different radiation angles of a narrowband Gaussian pulse were obtained by: (i) direct calculation using the slot-array FDTD model and time-domain near-to-far-field transformation and (ii) the convolution of the pulse signal and the AFFIR. The waveforms obtained using these approaches agree very well. This provides evidence that the far-field waveforms of any other radar pulse

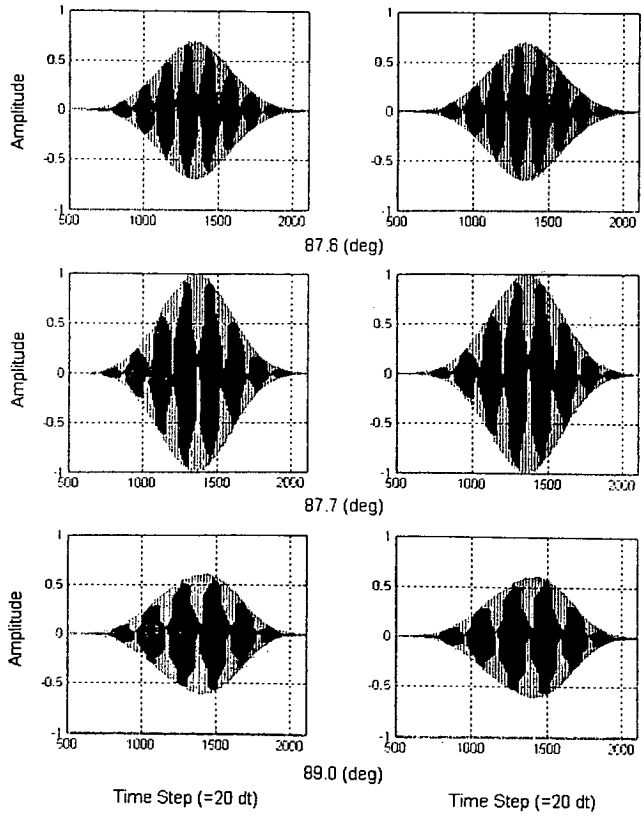

Figure 12 The $E_\phi(\phi, t)$ far-field waveforms at ϕ = 87.6°, 87.7°, and 89.0°

transmitted by the slot array can be calculated by simply realizing the convolution of the pulse signal and the AFFIR. Future work will apply this approach to obtain the far-field impulse response of other radar antennas or arrays and to investigate the characteristics of the far-field waveforms of different radar signals.

REFERENCES

1. L.B. Felsen, Transient electromagnetic fields, Springer-Verlag, Berlin, Heidelberg, 1976.
2. J.G. Maloney, G.S. Smith, and W.R. Scott, Jr., Accurate computation of the radiation from simple antennas using the finite-difference time-domain method, IEEE Trans Antennas Propagat 38 (1990), 1059–1068.
3. J. Tsui, Digital techniques for wideband receivers, Artech House, Boston, 2001.
4. K.S. Yee, Numerical solution of initial boundary value problems involving Maxwell's equations in isotropic media, IEEE Trans Antennas Propagat 14 (1966), 302–307.
5. E.A. Kraut, J.C. Olivier, and J.B. West, FDTD solution of Maxwell's equations for an edge slot penetrating adjacent broadwalls of a finite wall thickness waveguide, IEEE Trans Antennas Propagat 42 (1994), 1646–1648.
6. A. Taflove and S.C. Hagness, Computational electrodynamics: The finite-difference time-domain method, Artech House, Boston, 2000.
7. A.W. Rudge, K. Milne, A.D. Olver, and P. Knight, The handbook of antenna design, Peter Peregrinus Ltd., London, 1983.
8. W.H. Watson, The physical principles of waveguide transmission and antenna system, Oxford University Press, Oxford, 1947.
9. R.S. Elliott, Antenna theory and design, Prentice-Hall, New Jersey, 1981.
10. R.S. Elliott, The design of waveguide-fed slot arrays, Antenna handbook, Y.T. Lo and S.W. Lee (Editors), Van Nostrand Reinhold, Boston, 1993, ch. 12.
11. J. Berenger, A perfectly matched layer for absorbing of electromagnetic waves, J Computat Phys 114 (1994), 185–200.
12. E.A. Navarro, C. Wu, P.Y. Chung, and J. Litva, Application of PML superabsorbing boundary condition to nonorthogonal FDTD method, Electron Lett 30 (1994), 1654–1656.
13. R.C. Johnson and H. Jasik, Antenna engineering handbook, McGraw-Hill, New York, 1993.
14. M.I. Skolnik, Radar handbook, McGraw-Hill, New York, 1970.

RESONANT NONLINEARITY IN YTTERBIUM-DOPED DOUBLE-CLAD FIBER BRAGG GRATING

Lijun Li, Yange Liu, Xiujie Jia, Yanli Jin, Shuzhong Yuan, and Xiaoyi Dong
Institute of Modern Optics
Nankai University
Tianjin, P.R. China

Received 26 August 2005

ABSTRACT: *The resonant nonlinearity of a Ytterbium-doped double-clad fiber Bragg grating is investigated experimentally. The grating is formed in the hydrogen-loaded Ytterbiun-doped double-clad fiber using the phase-mask method. As the output mirror of the laser, this grating is spliced to the same active double-clad fiber. The residual pump power of a 976-nm laser is used to induce resonant nonlinearity of the Yb^{3+}-doped double-clad fiber Bragg grating and the central wavelength of the grating shifts nearly 0.2 nm in our experiment. This experiment demonstrates that the Ytterbium-doped double-clad fiber Bragg grating has a high nonlinearity coefficient.* © 2006 Wiley Periodicals, Inc. Microwave Opt Technol Lett 48: 430–432, 2006; Published online in Wiley InterScience (www.interscience.wiley.com). DOI 10.1002/mop.21371

Key words: *double-clad fiber; resonant nonlinearity; fiber Bragg grating; Ytterbiun-doped*

1. INTRODUCTION

Rare-earth-doped double-clad fibers (DCFs), which allow virtually the entire incident pump power to be launched into and guided within an inner cladding, are widely used in the fabrication of high-power fiber lasers. It is evident that laser compatibility and compactness can be improved if Bragg gratings are fabricated directly in the rare-earth-doped DCF as a laser medium [1–3]. Double-clad fiber Bragg gratings acting as important fiber-optic devices are formed directly in the rare-earth-doped DCF. They have been used for spectral filtering, wavelength tuning, and sensing [4], all of which have profited from the linear character of the DCF Bragg grating. However, because the DCF Bragg gratings are used in high-power lasers, it is necessary to research the nonlinearities (especially resonant nonlinearity) in rare-earth-doped fiber grating [5, 6].

In this paper, we present an experimental study on resonant nonlinearity in a Ytterbiun-doped double-clad fiber Bragg grating. The grating is formed in a hydrogen-loaded Ytterbiun-doped DCF using the phase-mask method. This grating is spliced to the same active DCF as the output mirror of the laser. There is a mass of residual pump laser existing at the output end of the laser. We use this residual pump laser to induce resonant nonlinearity in the DCF Bragg grating. The output spectrum of laser with various incident powers of a 976-nm laser is recorded. The laser central wavelength shifts nearly 0.2 nm, as does the DCF Bragg grating. This experiment demonstrates that the Yb^{3+}-doped DCF Bragg grating has a high nonlinearity coefficient.

2. THEORY

In a material with an intensity-dependent refractive index, the refractive index n can be written as follows:

$$n = n(I) = n_1 + \Delta n(I(x, y, z)), \tag{1}$$

where I is the intensity and x, y, and z define the position in the fiber. Nonlinearity due to the Kerr effect is described by the above equation with

$$\Delta n(I(x, y, z)) = n_2 I(x, y, z), \tag{2}$$

where n_2 is the nonlinear parameter, which can be used to express the nonlinear intensity of the fiber.

The resonant nonlinearity effect in fiber Bragg grating is that the refractive index of the signal-wave light changes through the variety of other wavelengths' light intensity. That is to say, I in Eq. (1) is not the intensity of the signal light itself. In rare-earth-doped fibers, the refractive index at a given wavelength is affected by a number of different transitions, even though they may be centered at relatively distant parts of the spectrum. By pumping the fiber at a suitable wavelength, resonant nonlinear processes can be produced. Taking the case of Yb^{3+}-doped DCF, the energy level structure consists of ${}^2F_{7/2} - {}^2F_{5/2}$ states corresponding to infrared absorption at 976 nm. So the absorption of the pump light at 976 nm will result in an associated change in the refractive index of the signal wavelength in the Yb^{3+}-doped DCF Bragg grating [5, 6].

The Bragg reflection wavelength is given by